J Mater Sci (2024) 59:9437–9454

Electronic materials

Role of interfacial layer as PANI–silicene in Si-based photodiodes

Adem Kocyigit[1], Dilber Esra Yıldız[2,*], Nevin Taşaltın[3,4,5,6,*], and Murat Yıldırım[7]

[1] *Department of Electronics and Automation, Vocational High School, Bilecik Şeyh Edebali University, 11000, Bilecik, Turkey*
[2] *Department of Physics, Hitit University, 19030 Çorum, Turkey*
[3] *Environment and Energy Technologies Research Center, Maltepe University, 34840 Istanbul, Turkey*
[4] *Department of Basic Sciences, Maltepe University, 34840 Istanbul, Turkey*
[5] *Department of Renewable Energy Tech. and Management, Maltepe University, 34840 Istanbul, Turkey*
[6] *CONSENS Inc., Maltepe University Research Center, Technopark Istanbul, 34840 Istanbul, Turkey*
[7] *Department of Biotechnology, Faculty of Science, Selcuk University, 42130 Konya, Turkey*

Received: 15 February 2024
Accepted: 11 May 2024
Published online: 28 May 2024

ABSTRACT

Silicene is a 2D monoatomic sheet of silicon and can be used for various applications such as degradation, therapy, and biosafety. Polyaniline (PANI) is a conducting polymer employed for electronic devices. In this study, we synthesized PANI–silicene composites and operated as an external interfacial layer between Al and different type substrates of *p*-Si and *n*-Si to compare Schottky-type photodiodes of PANI–silicene/*n*-Si and PANI–silicene/*p*-Si. The silicene structures were investigated using X-ray diffractometry (XRD) and scanning electron microscopy (SEM) techniques. Also, the light power intensity dependent of PANI–silicene/*n*-Si and PANI–silicene/*p*-Si photodiodes carried out in the range 0–100 mW/cm^2 and *I–t* measurements utilized to determine the response time of the photodiodes. Basic parameters of devices such as ideality factors barrier, height, and series resistance were obtained by Norde and Cheung methods and thermionic emission (TE) theory from *I–V* graphs. While the PANI–silicene/*n*-Si exhibited high ideality factor values of 5.49, the PANI–silicene/*p*-Si photodiodes showed a low ideality factor of 1.48. The photodiode parameters such as detectivity and responsivity were calculated as 6.40×10^9 Jones and 38.9 mA/W for *n*-Si substrate and 78.2 mA/W and 8.81×10^9 Jones for *p*-Si substrate. The case of basic electrical properties for PANI–silicene composite interlayer-based photodiodes was analyzed in detail.

Handling Editor: David Cann.

Address correspondence to E-mail: desrayildiz@hitit.edu.tr; nevintasaltın@maltepe.edu.tr

https://doi.org/10.1007/s10853-024-09782-3

Introduction

It is well known that silicene is a two-dimensional allotrope of silicon, and it is similar to graphene but composed of silicon atoms to be arranged in a honeycomb lattice, and it is a single layer of atoms, just like graphene, making it a nanomaterial with unique properties and potential applications [1]. The Poisson ratio of graphene is lower than silicene and also the ultimate stress, the bulk modulus, and the Young's modulus of silicene are obtained to be lower than for graphene [2]. While in-plane stiffness constant (C), and Poisson ratio (ν) are 62 J/m^2 and 0.3 for silicene, 335 J/m^2 and 0.16 for graphene, respectively [2, 3]. The graphene bulk modulus is determined to be 3.5 times higher than silicene [3, 4]. Silicene and graphene have unique band structure features, and there are conduction and valence bands, both of which have linear distributions, intersecting at the Brillouin region, the points K and K_0, and Fermi energy. It is reported that the silicene has two different band structures buckled and flat. Both forms of silicene have a zero π–π^* gap at the K point and electronic properties like graphene [3, 5, 6]. Electronic properties of silicene also enable to use of various devices such as photodiodes and photodetectors. Its direct bandgap in certain configurations allows for efficient light emission and absorption, which is crucial for developing efficient optoelectronic devices [7, 8].

In recent years, conductive polymers have attracted the attention of researchers due to their high conductivity [9, 10]. Thus, conductive polymers have been used frequently in device applications such as energy storage devices, supercapacitors, organic solar cells (OSCs), light-emitting diodes, sensors, etc. [11–19]. PANI is also a fascinating and versatile polymer belonging to the family of conducting polymers. Because it is renowned for its unique combination of electrical conductivity and processability, many researchers commonly studied PANI in the field of materials science [20]. PANI has been used in applications across various industries, including electronics, energy storage, corrosion protection, sensors, and biomedical devices [21]. In electronic devices, it has been used as a component in capacitors, batteries, and electromagnetic shielding due to its high electrical conductivity [22]. Due to ongoing research and advancements in polymer science, PANI continues to attract the attention of researchers to explore new ways to tailor its properties and applications. Its combination of electrical conductivity, tunable behavior, and ease of synthesis make PANI a versatile and promising material for a wide range of future technologies [23].

The Schottky barrier helps in efficient and fast carrier collection, resulting in rapid response times and high-speed operation of Schottky photodiodes compared to traditional p–n junction photodiodes [24]. These behaviors of the Schottky photodiode such as fast response and low noise make suitable applications for optical communication systems, fiber-optic communication networks, laser rangefinders, high-frequency and high-speed applications, and high-speed photodetector [25, 26]. As soon as enough energy strikes the surface of the Schottky photodiode near to metal, it generates hole-electron pairs in the semiconductor. Then, these hole-electron pairs are separated and collected due to the existence of the Schottky barrier [27]. The external interlayers such as conjugated polymer, metal complex ligands, or biomaterials are used in Schottky photodiodes to improve their performance and enhance their spectral sensitivity range [28, 29]. The interlayers provide spectral sensitivity adjustment, reduce dark current for high signal-to-noise ratio, increase responsivity, passivate surface dangling bonds, and barrier height adjustment [30]. Yıldırım et al. used propolis between n-Si and Au for UV-photodetector, and they reached 0.113 A/W responsivity and 4.04×10^9 Jones detectivity values [31]. Havigh et al. employed matrix-polymer of carbon and polyvinylpyrrolidone (PVP) composites for UV–Vis photodetector applications, and they obtained 0.69 A/W responsivity, 5.60×10^{10} Jones detectivity and 53.76×10^3 on–off ratio for UV region [32]. Imer et al. investigated Ru(II)-pydim complex as an interface layer between p-Si and Al for photodetection applications. The authors achieved 0.131 A/W responsivity and 1.63×10^{11} Jones detectivity values for visible light [33].

In this study, we synthesized PANI-silicene composites and used an external interfacial layer between Si (for n-type and p-type) and Al to accomplish the Al/PANI–silicene/n-Si and Al/PANI–silicene/p-Si photodiodes. Detailed characterization and comparison were performed based on various diode parameters, detectivity, and responsivity for fabricated photodiodes in detail.

Material and method

The utilized semiconductor wafers were oriented (100) crystalline plane for *p*-type Si and *n*-type Si with resistivity ranging from 1 to 10 Ω cm, carrier concentrations of 7.5×10^{16} cm^{-3}, and thicknesses of 400 µm. They were then cut into 2 cm^2 pieces and underwent a cleaning process using an ultrasonic cleaner with isopropanol and acetone. To eliminate the SiO_2 layer formed on the silicon wafer's surface due to Si–O interactions, the pieces were briefly immersed into a solution of HF:H_2O (1:1) for 30 s, and subsequently dried with nitrogen. A thermal evaporator was employed to obtain back contacts on the back of the pieces with 100 nm Al metal under pressure of 5×10^{-6} torr. Following this, the *n*-Si/Al and *p*-Si/Al structures were annealed at 550 °C in a nitrogen atmosphere for 10 min to achieve ohmic contact. For preparing the silicene, physical exfoliation of 100 mg Si microparticles was performed by sonicating in a mixture of 100 mL deionized water and isopropanol with an equal volume in a nitrogen flow-controlled cabin for 4 h. Centrifugation at 5000 rpm and 12000 rpm were subjected to the resulting Si particles for 15 min, then the collected silicene was left to dry at 50 °C in a vacuum oven. For obtaining PANI-silicene composites, the silicene and PANI were individually mixed in 2 mL of N-methyl-2-pyrrolidone (NMP) solution each of 1 mg, and sonicated for 5 min [34]. The solution was applied in three layers onto the *n*-Si/Al and *p*-Si/Al samples using a spin coater at 2000 rpm rotating speed for 40 s. Subsequently, the PANI-silicene/*p*-Si and the PANI-silicene/*n*-Si were conveyed to a thermal evaporation system, where another Al metal with 100 nm thickness was deposited onto them through a hole array mask with 7.85×10^{-3} cm^2 areas. This process was employed to obtain rectifying Schottky contacts. Figure 1a depicts the visual representation of the fabricated devices with a measurement system, and Fig. 1b shows a schematic energy band diagram. As seen in

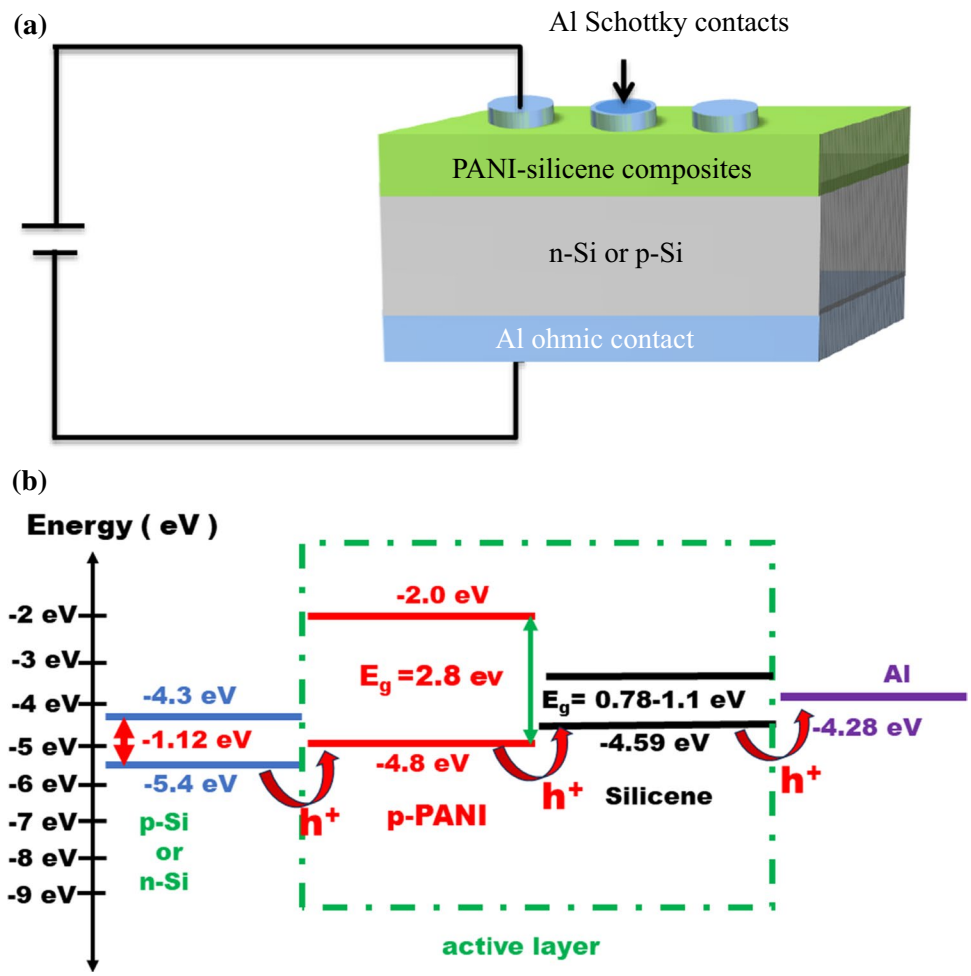

Figure 1 **a** The visual representation of the measurement system along with the created devices and **b** schematic energy band diagram of Al/PANI-silicene/*p*-Si or *n*-Si devices.

Fig. 1b, PANI, has low band energy (E_g = 2.8 eV); as a result, it can be activated in visible light [35]. In addition, the band structure of silicene (in the absence of spin–orbit interaction) has a zero gap at the Fermi energy, and the work function of silicene is 4.59 eV [36, 37]. According to the simulation model of the new silicene crystal with the rectangular lattice related to the experimental result, the energy band structure is calculated, and a real direct bandgap of silicene is 0.78 (for silicene crystal with the rectangular lattice related)—1.11(for zigzag dumbbell silicene) eV [38, 39]. Here, the different bandgap from that in the silicene crystal with the hexagonal lattice may be due to the difference in combining energy. Moreover, the interesting electronic properties of the lowest energy 2D polymorphs of silicene make them promising candidates for optoelectronic applications.

Malvern Panalytical Aeris X-ray diffractometry (XRD) operated at 600 W was employed for the crystalline structure of silicene. SEM images of the silicene were taken by ZEISS EVO LS10 with Bruker energy-dispersive X-ray spectroscopy (EDS) detector. The obtained devices underwent characterization using the Fytronix FY-7000 measurements system, where *I–t* (current–time) and *I–V* (current–voltage) measurements were conducted under dark and illumination. This characterization process allowed for a comprehensive understanding of the electrical behavior and performance of the devices in different light conditions.

Results and discussion

The crystallinity of the prepared silicenes was examined by XRD analysis (Fig. 2). As shown in Fig. 2, the peaks of (111), (220), and (311) at the XRD pattern of silicene can correspond to Fd-3m (227) space group centrosymmetric cubic crystal. These results are in good agreement with JCPDS Card No. 73-1665 and confirm the silicene structure. The a, b, and c parameters for the unit cell were determined as 5.431 Å, 5.431 Å, and 5.431 Å, respectively. In the previous article, Baytemir et al. [34] indicated that the silicene nanosheet has a hexagonal honeycomb lattice structure using an HRTEM image, and Yildiz et al. reported that the FTIR of PANI-silicene composites is similar to PANI [40].

The surface morphology of the PANI-silicene film on the Si surface are shown in Fig. 3a and b from cross

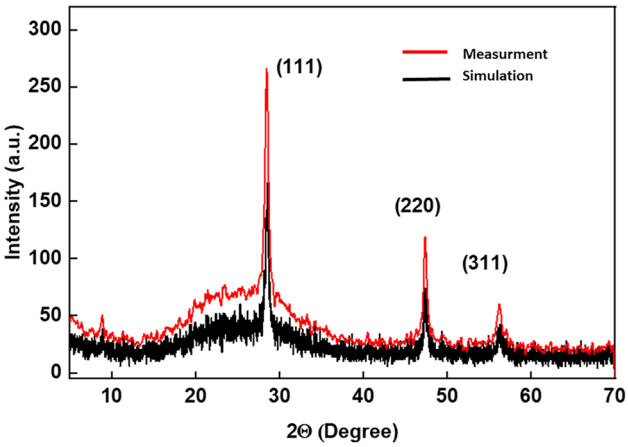

Figure 2 XRD pattern of the silicene structures.

section. The silicon substrate and PANI-silicene layer can be seen in Fig. 3a with approximately 300 nm thicknesses. The morphology of the surface looks almost homogenous for a wide area. Figure 3b shows the EDS region on SEM images. Figure 3c displays the EDS spectrum and the weighted atomic and molecular distribution of the silicene layer. The C, N, and Si are detected from the EDS spectrum. These results can be confirmed for PANI and silicene, separately by previous literature [41, 42].

The work functions of the *p*-Si, *n*-Si, and Al are 4.1 eV, 4.6 eV, and 4.3 eV, respectively. By these values, rectifying contact between Al and *p*-Si can easily be composed because metal has a higher work function value than semiconductor. However, it is hard to compose a rectifying contact between Al and *n*-Si. The external PANI-silicene layer or natural oxide layer between Si and O can help to compose barrier height or rectifying property. Figure 4 indicates *I–V* plots of Al/PANI–silicene/*p*-Si and Al/PANI–silicene/*n*-Si photodiodes. Figure 4a and c shows *I–V* of Al/PANI–silicene/*n*-Si for forward and reverse biases, respectively. The current increased by increment voltage and light power density at forward and reverse biases. Normally, reverse bias currents of a diode are around μA level instead of mA level. The high reverse bias current and increasing current with voltage can be attributed to the conducting behavior of PANI and non-forming a good rectifying behavior. However, the Al/PANI–silicene/*n*-Si heterojunction can be thought of as a photodetector due to the high increase in the level of photocurrent at forward and reverse biases. Figure 4b and d shows *I–V* plots

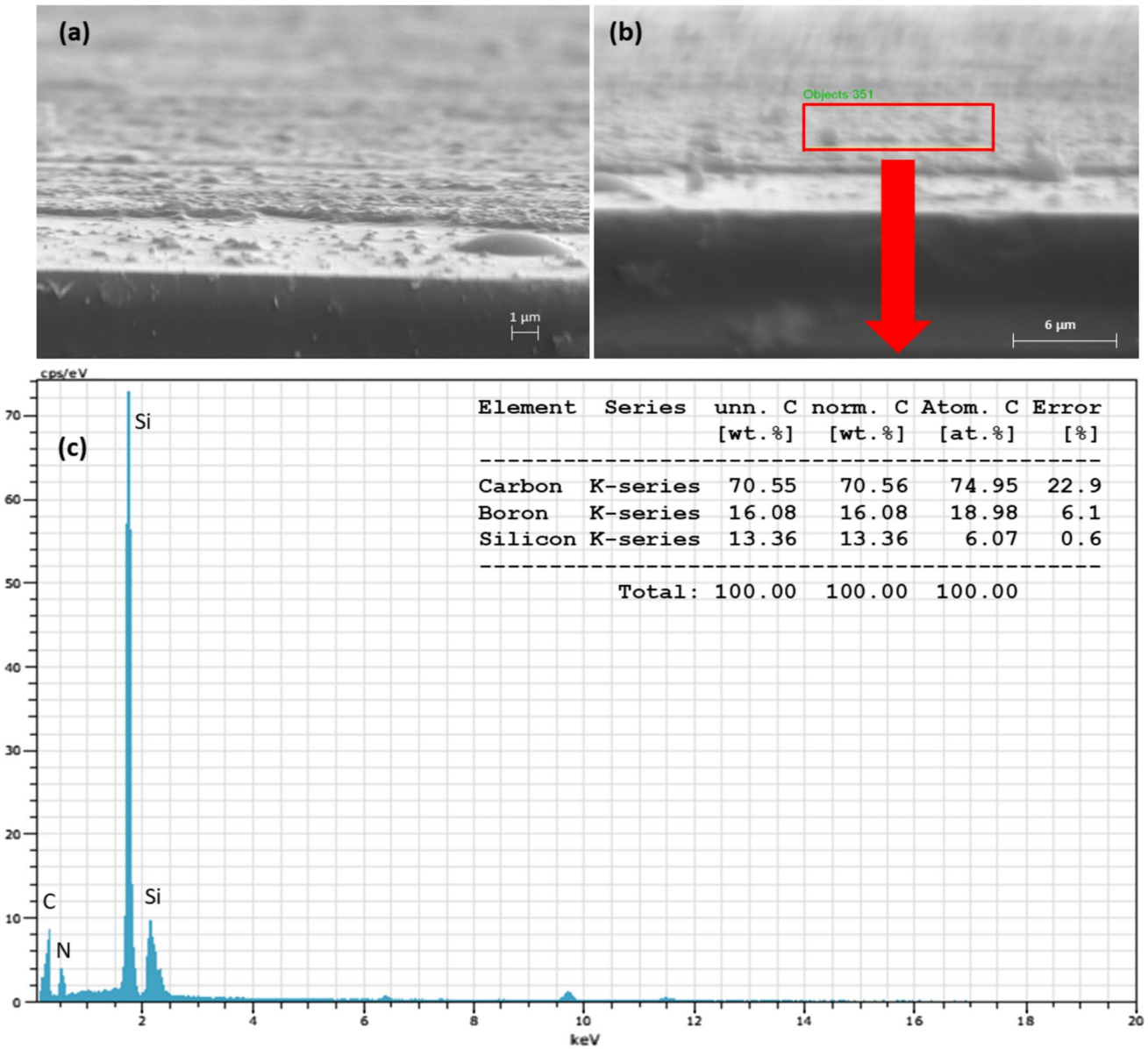

Figure 3 **a** SEM image of the silicene film on the Si substrate. **b** SEM image of the surface for EDS square. **c** EDS spectrum of the silicene square part of **b**.

of the Al/PANI–silicene/*p*-Si for forward and reverse biases. With an increase in light power intensity under both forward and reverse biases, the current values demonstrated an upward trend. However, the current values reached a constant value both at reverse biases (around − 0.20 and − 0.50 V) and forward biases (around 1.50 and 1.80 V). While the reverse bias characteristics clearly exhibit a photodiode characteristic, the forward bias characteristics indicate a phototransistor-like characteristic. This kind of behavior can be attributed to the external PANI-silicene layer [43]. The determined threshold voltages of Al/PANI–silicene/*n*-Si and Al/PANI–silicene/*p*-Si photodiodes are 0.70 and 0.25 V, respectively. The high threshold values of the photodiode with *n*-Si semiconductor according to the photodiode with *p*-Si can be attributed to work function differences [44, 45].

Figure 5a and b displays the ln *I*–*V* plots of the Al/PANI–silicene/*p*-Si and Al/PANI–silicene/*n*-Si photodiodes, respectively. These plots represent the characteristics of the devices under different light power densities, ranging from dark conditions to 100 mW/cm^2 by

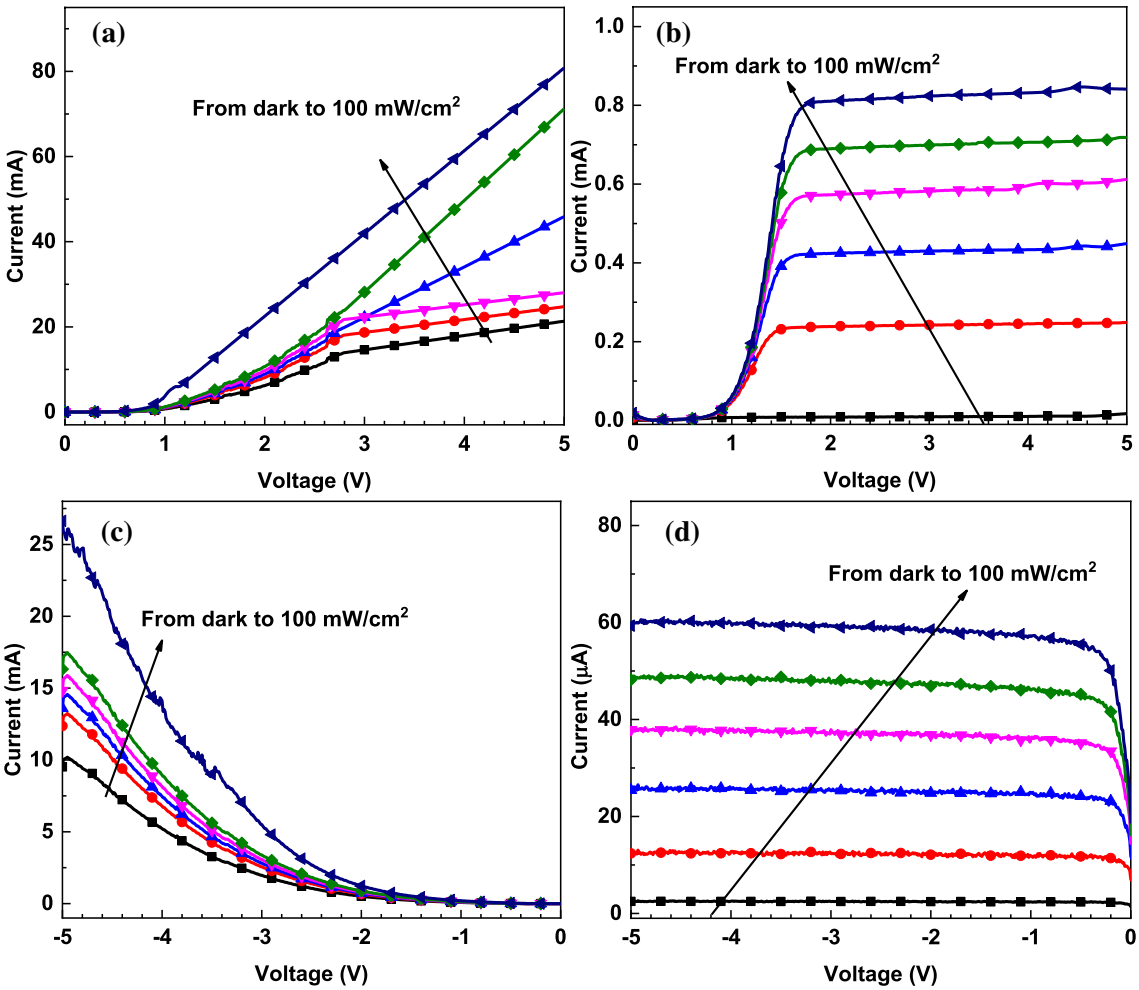

Figure 4 The forward biases *I–V* plots for **a** Al/PANI–silicene/*n*-Si and **b** Al/PANI–silicene/*p*-Si photodiodes, revere biases *I–V* plots of **c** Al/PANI–silicene/*n*-Si and **d** The revere biases of Al/PANI–silicene/*p*-Si photodiodes.

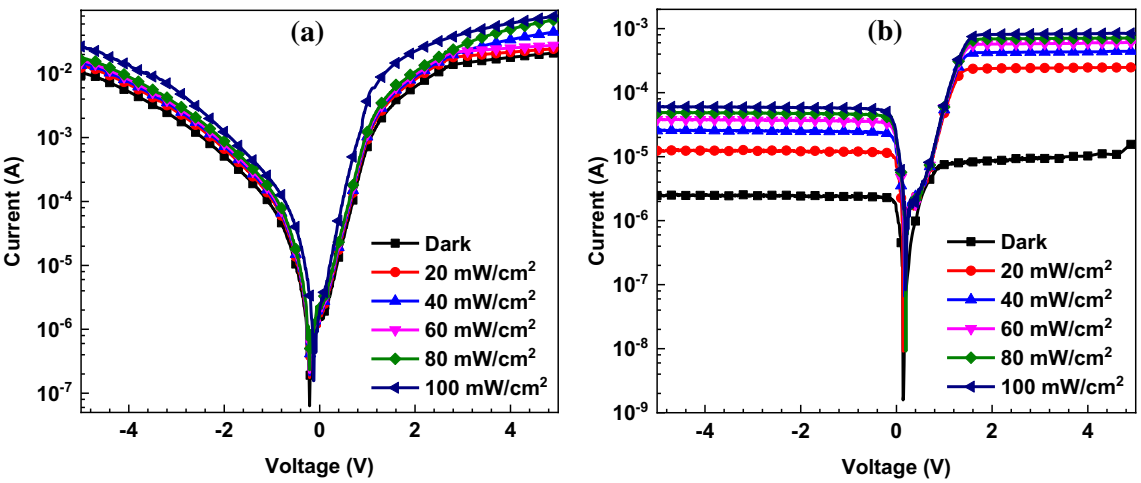

Figure 5 ln *I–V* plots of the **a** Al/PANI–silicene/*n*-Si and **b** Al/PANI–silicene/*p*-Si photodiodes.

20 mW/cm^2 intervals. According to Fig. 3, both photodiodes gave the response to increasing light power for reverse and forward biases due to the effect of external layers of PANI-silicene composites as well as the metal–semiconductor interface [46]. Furthermore, the displacement of the *I–V* characteristics toward the positive voltage region under the influence of light can be ascribed to the augmentation of charge carriers in the interface of the devices caused by the density of light power [47].

Diverse device parameters can be derived from the semi-logarithmic *I–V* characteristics using the techniques, including TE theory, Norde, and Cheung methods [48]. The expression of current can be found below depending on the saturation current (I_0), ideality factor (n), Boltzman constant (k), charge of electron (q), medium temperature (T), and voltage (V) [49, 50]:

$$I = I_0 \exp\left(\frac{qV}{nkT}\right)\left[-\exp\left(-\frac{qV}{kT}\right)\right] \tag{1}$$

where I_0 is given by following equation depending on Richardson constant (A^*) for 32 A/cm^2 K^2 in the case of *p*-type Si and 112 A/cm^2 K^2 for *n*-type Si, barrier height (Φ_b), device area (A), k and T.

The I_0 values were determined from semi-logarithmic *I–V* plots of the Al/PANI–silicene/*n*-Si and Al/PANI–silicene/*p*-Si photodiodes and given in Table 1. The I_0 values exhibited variations when the substrate types were changed, attributed to differences in work functions for *p*-Si and *n*-Si substrates. By using saturation current, the barrier height and ideality factor can be calculated by following equations for $V \geq 3kT/q$ [51, 52]:

$$I_0 = AA^*T^2 \exp\left(-\frac{q\phi_b}{kT}\right) \tag{2}$$

The values of Φ_b and n formulas $V \geq 3kT/q$ can be determined by following formulas by help of above equations:

$$n = \frac{q}{kT}\left(\frac{dV}{d\ln I}\right) \tag{3}$$

and

$$\phi_b = \frac{kT}{q}\ln\left(\frac{A^*AT^2}{I_0}\right) \tag{4}$$

The obtained Φ_b and n values are tabulated in Table 1 both the Al/PANI–silicene/*n*-Si and Al/PANI–silicene/*p*-Si photodiodes at dark measurements conditions. When Al/PANI–silicene/*n*-Si has a high value ideality factor of 5.49, the Al/PANI–silicene/*p*-Si has a low value of 1.46. The high n values can depend on interface states, the presence of an external interfacial layer, barrier inhomogeneity, or series resistance [53, 54]. The Φ_b values of Al/PANI–silicene/*n*-Si and Al/PANI–silicene/*p*-Si photodiodes were determined to be 0.70 and 0.83 eV, respectively. The differences in the Φ_b values for changing substrate types can be depended on the work function differences. The changes at the Φ_b and n values for increasing light power density of the Al/PANI–silicene/*n*-Si and Al/PANI–silicene/*p*-Si photodiodes are introduced in Fig. 6a and b, respectively. As the light power density increased, the n values showed a linear rise, while the Φ_b values exhibited a general decrease. The increasing n values could be attributed to elevated barrier inhomogeneity or interface states and a reduction in series resistance because of an influx of charge carriers at the diode interfaces [55]. Additionally, the decreasing trend in Φ_b values could be attributed to an increase in saturation currents as well as the photocurrent of the diodes. However, the increment at the n values and decrement at the Φ_b values of Al/PANI–silicene/*n*-Si changed slightly. This result also can be ascribed to work function variations between Al metal and Si semiconductors. In other words, work function differences between Al with *p*-Si and *n*-Si caused an effect on the transition of the current in the junction, and thus both Φ_b and n values exhibited different changing profiles with light power density [56].

Table 1 The device parameters of the PANI–silicene/*n*-Si and PANI–silicene/*p*-Si photodiodes

Substrate type	Saturation current (I_0)	n (*I–V*)	n Cheung	ϕ_b (*I–V*) (eV)	ϕ_b Cheung (eV)	ϕ_b Norde (eV)	R_s Cheung (kΩ-*H*(*I*))	R_s Cheung (kΩ-d*V*/dln*I*)	R_s Norde (kΩ)
n-type	1.23×10^{-7}	5.49	5.51	0.70	0.66	0.76	0.10	0.22	0.03
p-type	2.29×10^{-10}	1.46	1.38	0.83	0.84	0.86	39.31	37.72	122.13

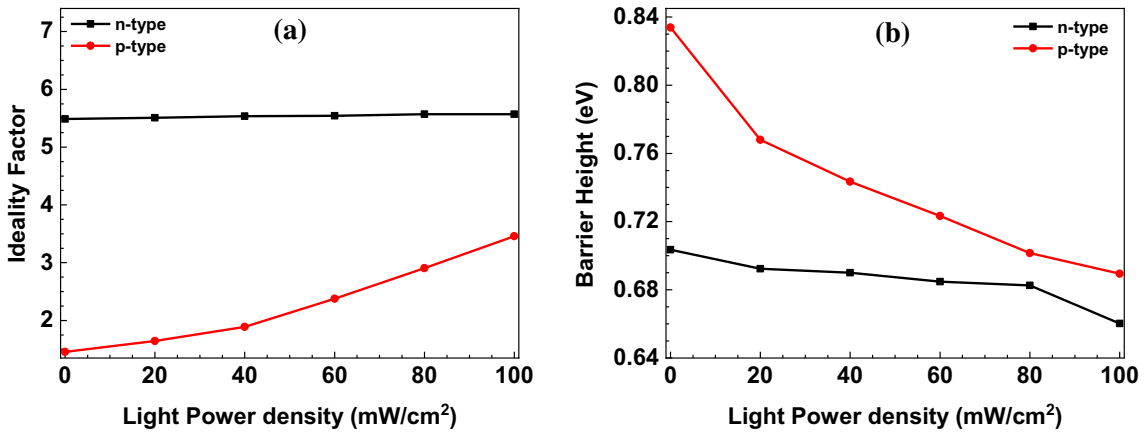

Figure 6 **a** The ideality factor and **b** barrier height changes of Al/PANI–silicene/*n*-Si and Al/PANI–silicene/*p*-Si photodiodes depending light power density.

The obtained results can be compared with previous literature for various Schottky devices. Some researchers employ Si as be semiconductor, others use ITO, GaAs, etc. Haciismailoglu et al. fabricated Ni/n-GaAs Schottky diode (without interlayer) by electrodeposition technique for photovoltaic applications; they calculated ideality factor and barrier height to be 1.05 and 0.70 eV, respectively [57]. Barkhordari et al., employed PVP:$ZnTiO_3$ composites as an interlayer between Al and *p*-Si to obtain Schottky-type photodiodes, and they determined ideality factor and barrier height as 5.81 and 0.687 eV [58]. Wang et al. fabricated Gr/GO/*n*-Si Schottky silicon photodiode and obtained the ideality factor and barrier height of the device to be 2.19 and 0.88 eV [59]. Dhibar et al. reported that the charge transport behavior of metallohydrogel of Mg (II) ion using pentaethylenehexamine (PEHA) (Mg@PEHA)-based Schottky diode structures and displayed bipolar resistive switching behavior at room temperature for a resistive random-access memory (RRAM) device using Mg@PEHA. This device demonstrated excellent performance with a high ON/OFF ratio of approximately 100 and remarkable endurance of over 5000 switching cycles, but the ideality factor and barrier height of the ITO/Mg@PEHA/ITO device were calculated to be 51.83 and 0.026 eV [60]. Also, Karmakar et al. were indicated that the charge transport behavior Mg (II) metallohydrogel with trimethylamine (Mg@TMA) and Mg (II) metallohydrogel with 3-amino-1-propanol-based metallohydrogel (Mg@3AP)-based metal–semiconductor–metal structures and displayed bipolar resistive switching behavior at room temperature for RRAM device using of Mg@TMA and Mg@3AP. These devices exhibited excellent switching endurance over 10,000 switching cycles with a large ON/OFF ratio (~ 100) for Mg@TMA [61] and Mg@3AP [62]. While the ideality factor values were obtained to be 0.84 for Mg@TMA and 0.70 for Mg@3AP, barrier height values obtained as 0.026 eV for both ITO/Mg@3AP/ITO and ITO/Mg@TMA/ITO devices. The calculated results of the ideality factor and barrier height in this study can be comparable with various Schottky diodes, especially Si semiconductors with interlayers.

The junction resistance (R_j) of the Al/PANI–silicene/*n*-Si and Al/PANI–silicene/*p*-Si photodiodes is determined by the relation of the d*V*/d*I*. Furthermore, it is important to know that R_j consists of both series resistance (R_s) and shunt resistance (R_{sh}). To ensure optimal performance of optoelectronic devices a low R_s and a high R_{sh} are essential. The R_{sh} values are obtained at reverse biases to achieve a constant or flat R_j graph, while the R_s values are chosen from the straight region of the R_j graph under positive voltage values [63]. In other words, if the R_j decreases and reaches a constant at a certain value of higher forward biases, the R_j values show R_s. However, constant R_j values represent R_{sh} values at high enough reverse biases. Figure 7a and b illustrates the R_j profile for Al/PANI-silicene/*n*-Si and Al/PANI-silicene/*p*-Si photodiodes at different densities of light powers, respectively. The trend shows a decrease in both R_{sh} and R_s values as the light power density increases, validating the correlation with changes in *n* and Φ_b values. Both R_s and R_{sh} values revealed horizontal regions for higher forward and reverse biases of the Al/PANI-silicene/*n*-Si and Al/PANI-silicene/*p*-Si photodiodes.

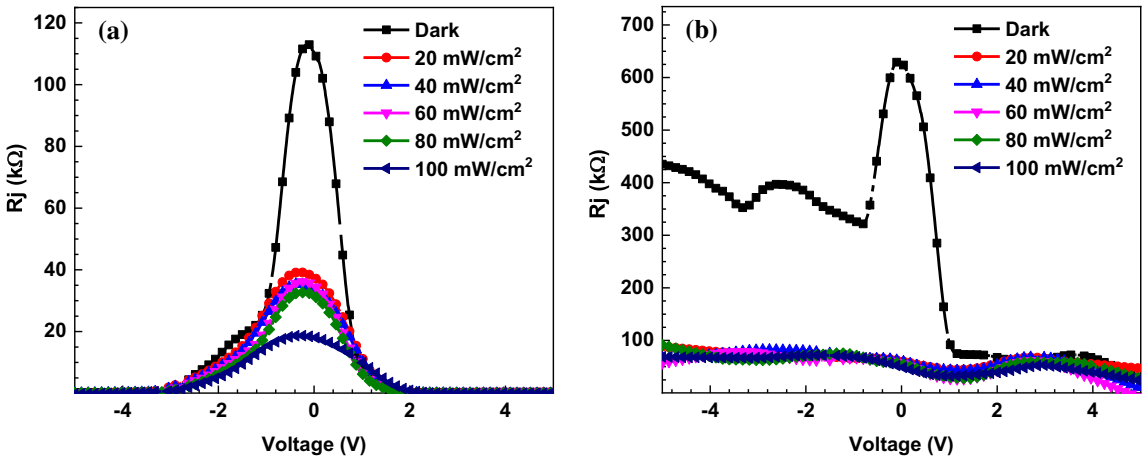

Figure 7 The R_j–V plots of the **a** Al/PANI–silicene/*n*-Si and **b** Al/PANI–silicene/*p*-Si photodiodes.

The R_{sh} and R_s values of the Al/PANI-silicene/*n*-Si are 10.95×10^3 Ω and 0.28×10^3 Ω, respectively. For the Al/PANI-silicene/*p*-Si photodiode, the R_{sh} and R_s values are 3.34×10^5 Ω and 70.92×10^3 Ω, respectively.

Another approach for determining the series resistance (R_s) and additional device parameters like n and Φ_b involves employing the Cheung method, which elucidates the current using the next equation correlated with the device's R_s value [64]:

$$I = I_0 \exp\left(-\frac{q(V - IR_s)}{nkT}\right) \tag{5}$$

where IR_s represents the voltage drop across the device attributed to R_s value. Utilizing Eq. (5), we derive two Cheung functions, which are expressed by the subsequent formulas:

$$\frac{dV}{d(\ln I)} = IR_s + n\frac{kT}{q} \tag{6}$$

$$H(I) = IR_s + n\phi_b \tag{7}$$

When plotting both $H(I)$ and $dV/d\ln I$ against current, linear plots emerge because of the inherent relationship between Cheung functions and current. The plot of $dV/d\ln I$ aids in determining the n value through the y-axis crossing point and one of the R_s value by the slope of the plot while the $H(I)$ against I plot facilitates extraction of another R_s and Φ_b values. The Cheung graphs of the Al/PANI–silicene/*n*-Si and Al/PANI–silicene/*p*-Si photodiodes are illustrated in Fig. 8a and b, respectively. The extracted n, R_s, and Φ_b values from the Cheung method are compiled in Table 1. Discrepancies between the TE theory and Cheung method values for Φ_b and n arise from non-ideal device structures and approximative variations [65]. Notably, the calculated R_s values align with the $H(I)$-I and $dV/d\ln I$-I graphs of each device, confirming the stability of the Cheung method [66]. Moreover, the R_s values for the Al/PANI–silicene/*n*-Si photodiode surpass those of the Al/PANI–silicene/*p*-Si counterpart because of interface states between Al metal and *n*-Si and greater barrier inhomogeneity in the interface. It is important to acknowledge that the disparities between directly calculated R_s values and those obtained through the Cheung method can be dependent on approximation variations [67].

The utilization of the Norde method presents an alternative means to enhance the consistency of diode parameters, allowing for the calculation of R_s and Φ_b. The Norde function is expressed by the next formula [67].

$$F(V) = \frac{V}{\gamma} - \frac{kT}{q}\ln\left(\frac{I(V)}{AA^*T^2}\right) \tag{8}$$

where γ represents an integer greater than n which is obtained by TE theory, and $I(V)$ signifies the current. The calculation of Φ_b and R_s values is accomplished through the following formulas derived from the Norde function:

$$\phi_b = F(V_0) + \left[\frac{V_0}{\gamma} - \frac{kT}{q}\right] \tag{9}$$

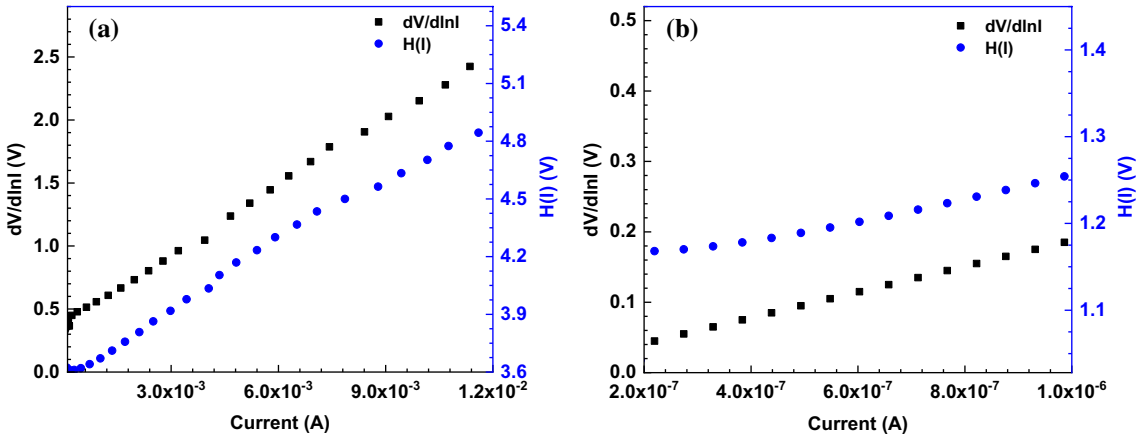

Figure 8 Cheungs plots of the **a** Al/PANI–silicene/*n*-Si and **b** Al/PANI–silicene/*p*-Si photodiodes.

$$R_s = \frac{\gamma - n}{I}\frac{kT}{q} \tag{10}$$

where V_0 is the minimum voltage value dependent minimum $F(V)$ value.

Figure 9a and b depicts the $F(V)$-V characteristics of Al/PANI–silicene/*n*-Si and Al/PANI–silicene/*p*-Si devices. The resulting Φ_b and R_s values are presented in Table 1, showcasing a favorable alignment with the calculated Φ_b and R_s values from both TE theory and the Cheung method. Minor divergences can be ascribed, once more, to non-ideal diode structure as well as inherent approximation discrepancies unique to each device, and similar results were indicated by other researchers [29, 68].

Current transient measurements of a photodiode provide crucial insights into their dynamic behavior and performance characteristics. These measurements involve monitoring the changes in current flow through the photodiode over time, typically in response to variations in incident light intensity or applied voltage. By analyzing these transient responses, various photodiode properties such as photosensitivity, responsivity, and speed of response can be understood. Figure 10a and b displays current transient graphs of the Al/PANI-silicene/*n*-Si and Al/PANI-silicene/*p*-Si photodiodes for light power on and off situations in 5 s at − 2 V, respectively. Both photodiodes have exhibited an immediately increasing profile when the light is on and a decreasing profile when the light is off.

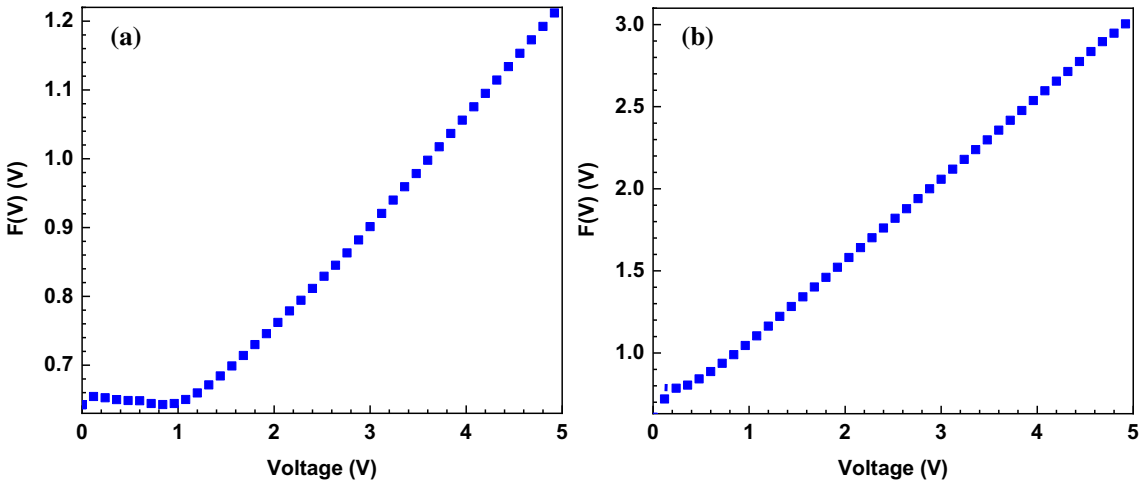

Figure 9 The $F(V)$–V graphs of the **a** Al/PANI–silicene/*n*-Si and **b** Al/PANI–silicene/*p*-Si photodiodes.

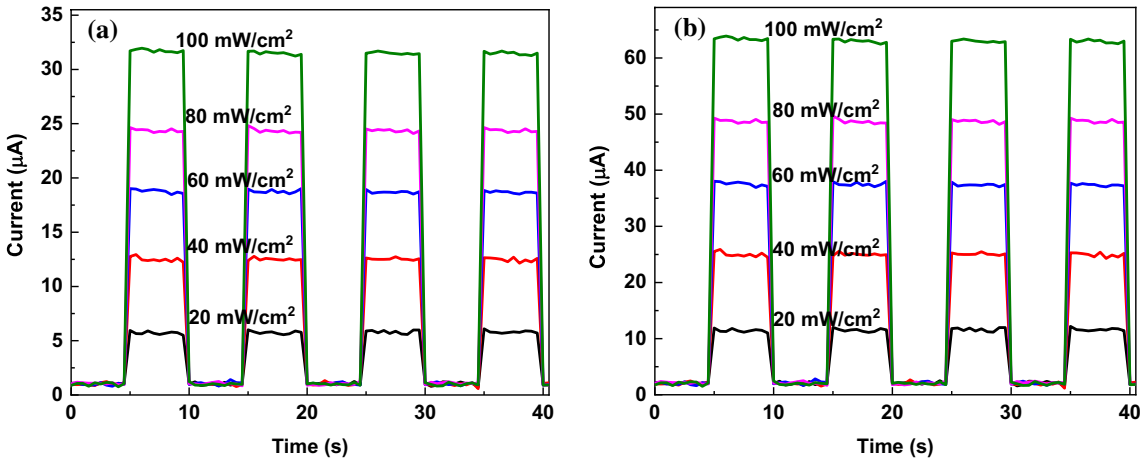

Figure 10 The *I–t* characteristics of the **a** Al/PANI–silicene/*n*-Si and **b** Al/PANI–silicene/*p*-Si photodiodes depending on light power density.

The response time of a photodiode shows reaction speed to changes in light power density, and it is an important parameter for detection performance [69]. Figure 11a and b shows the response time of Al/PANI–silicene/*n*-Si and Al/PANI–silicene/*p*-Si photodiodes for 100 mW/cm^2 light power density. Both devices exhibited 400 ms rise and fall times, implying fast photoresponse for optoelectronic applications.

In order to examine how photoconduction changes with varying illumination intensities, we constructed a double-logarithmic plot of photocurrent (I_{ph}) against light density (P). The underlying photoconduction mechanism can be investigated through the utilization of the below equation:

$$I_{ph} = \alpha P^m \tag{11}$$

where m stands for the power exponent, and α represents a constant. The m value is determined by the slope of LogI_{ph}–Log$P$ plots. If the m value is greater than unity and exhibits linear behavior, the related device reveals a photoconductive mechanism [70]. Power-dependent photoresponsivity and LogI_{ph}-Log$P$ plots of the Al/PANI–silicene/*n*-Si and Al/PANI–silicene/*p*-Si photodiodes are indicated in Fig. 12a and b, respectively. Both current and photoresponsivity have generally linear variations with increments of light power density. The m values were determined as 1.12 and 1.11 for Al/PANI–silicene/*n*-Si and Al/PANI–silicene/*p*-Si photodiodes, respectively.

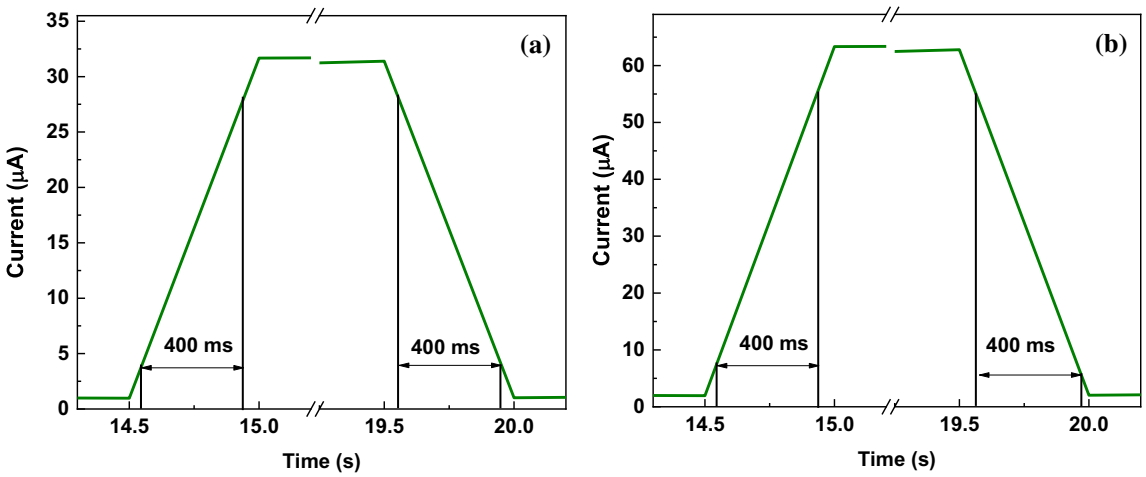

Figure 11 Response time of **a** Al/PANI–silicene/*n*-Si and **b** Al/PANI–silicene/*p*-Si photodiodes for 100 mW/cm^2 light power density.

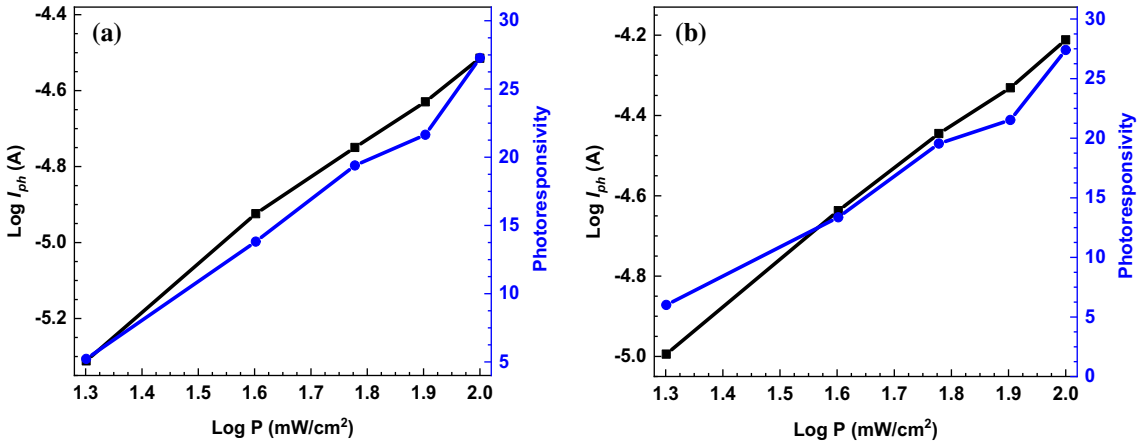

Figure 12 The LogI_{ph}–Log$P$ graphs of the **a** Al/PANI–silicene/*n*-Si and **b** Al/PANI–silicene/*p*-Si photodiodes.

These *m* values clearly confirmed that both devices can be used for applications of optoelectronic [71].

The responsivity serves as a key parameter for the effectiveness of a photodiode or photodetector, quantifying its sensitivity to incident light. This parameter can be mathematically expressed using the following equation [72]:

$$R = \frac{I_{\text{ph}}}{PA} \tag{12}$$

Figure 13a and b illustrates the alterations at responsivity of the Al/PANI–silicene/*n*-Si and Al/PANI–silicene/*p*-Si devices as a function of reverse biases, respectively. Notably, the responsivity of the Al/PANI–silicene/*p*-Si photodiode exhibited a rapid rise with minor reverse biases, followed by a relatively stable trend as the reverse biases increased. However, the responsivity of the Al/PANI–silicene/*n*-Si increased almost linearly by increasing reverse biases after − 2 V. While the responsivity level of the Al/PANI–silicene/*n*-Si is around 10^3 mA/W, the Al/PANI–silicene/*p*-Si photodiode has 10^2 mA/W level. Moreover, the responsivity of each device exhibited generally a rise in correspondence with increasing light power density. This phenomenon can be dependent on the generation of excitons at the photodiode interface [73]. The applied voltage plays a pivotal role in generating these excitons, thereby facilitating the enhancement of photocurrent within the photodiode interface.

While the rectifying ratio (*RR*) is important for diode characteristics, the photocurrent, responsivity,

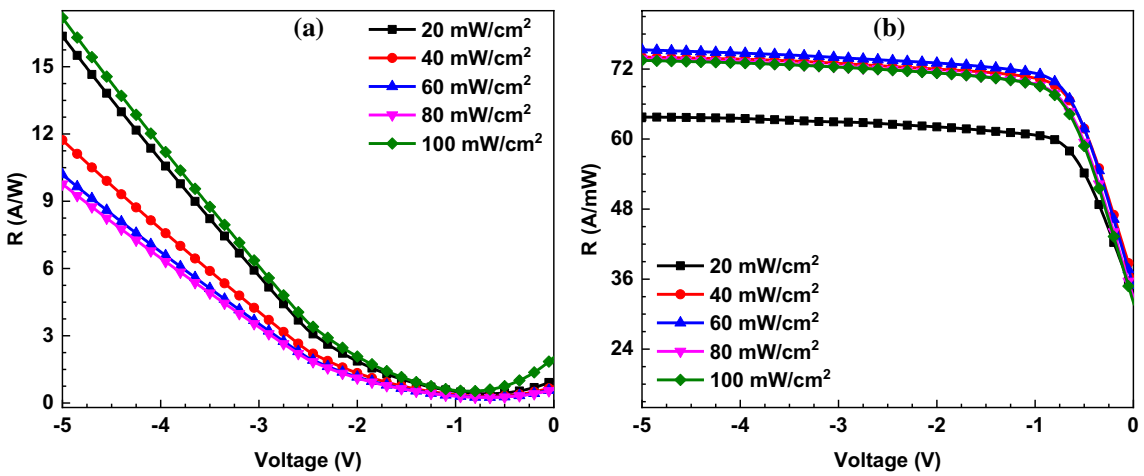

Figure 13 The *R*–*V* of the **a** Al/PANI–silicene/*n*-Si and **b** Al/PANI–silicene/*p*-Si photodiodes.

and specific detectivity are key parameters employed in the assessment of the properties of a photodiode characteristic. The *RR* is obtained ratio of the currents for the same voltages at forward and reverse biases. The *RR* profiles of the Al/PANI–silicene/*p*-Si and Al/PANI–silicene/*n*-Si photodiodes under varying light power densities are illustrated in Fig. 14a. The *RR* values of the Al/PANI–silicene/*p*-Si photodiode slightly increased with decreasing light power density after 20 mW/cm^2 because of rising current at reverse biases by power density of light. However, the *RR* values of the Al/PANI–silicene/*n*-Si photodiode stayed constant up to 20 mW/cm^2 and then increased slightly. The photocurrent of a photodiode is calculated by subtracting of illuminated current from dark currents. The alterations in photocurrent, influenced by changes in light power density, are depicted in Fig. 14b for the Al/PANI–silicene/*n*-Si and Al/PANI–silicene/*p*-Si photodiodes. Notably, the photocurrent values for both photodiodes displayed an almost linear increase with the increasing of light power. However, it is worth noting that the Al/PANI–silicene/*p*-Si photodiode exhibited notably higher photocurrent values in comparison. The responsivity of photodiodes shows sensitivity to the light. Figure 14c illustrates the responsivity profiles of the Al/PANI–silicene/*p*-Si and Al/PANI–silicene/*n*-Si photodiodes depending on light power density under a reverse bias of − 2 V. While both photodiodes exhibited a slight increase in responsivity with rising light power, it's notable that the Al/PANI–silicene/*p*-Si photodiode demonstrated higher responsivity values in comparison to the Al/PANI–silicene/*n*-Si photodiode. The specific detectivity of a photodiode represents to sense ability of the smallest signal that can be detected. Turning to Fig. 14d, the changes in detectivity due to increasing light power density are displayed for both the Al/PANI–silicene/*n*-Si and Al/PANI–silicene/*p*-Si photodiodes. Interestingly, the detectivity profiles of the two photodiodes exhibit similarities. Overall, the detectivity and responsivity values obtained from the

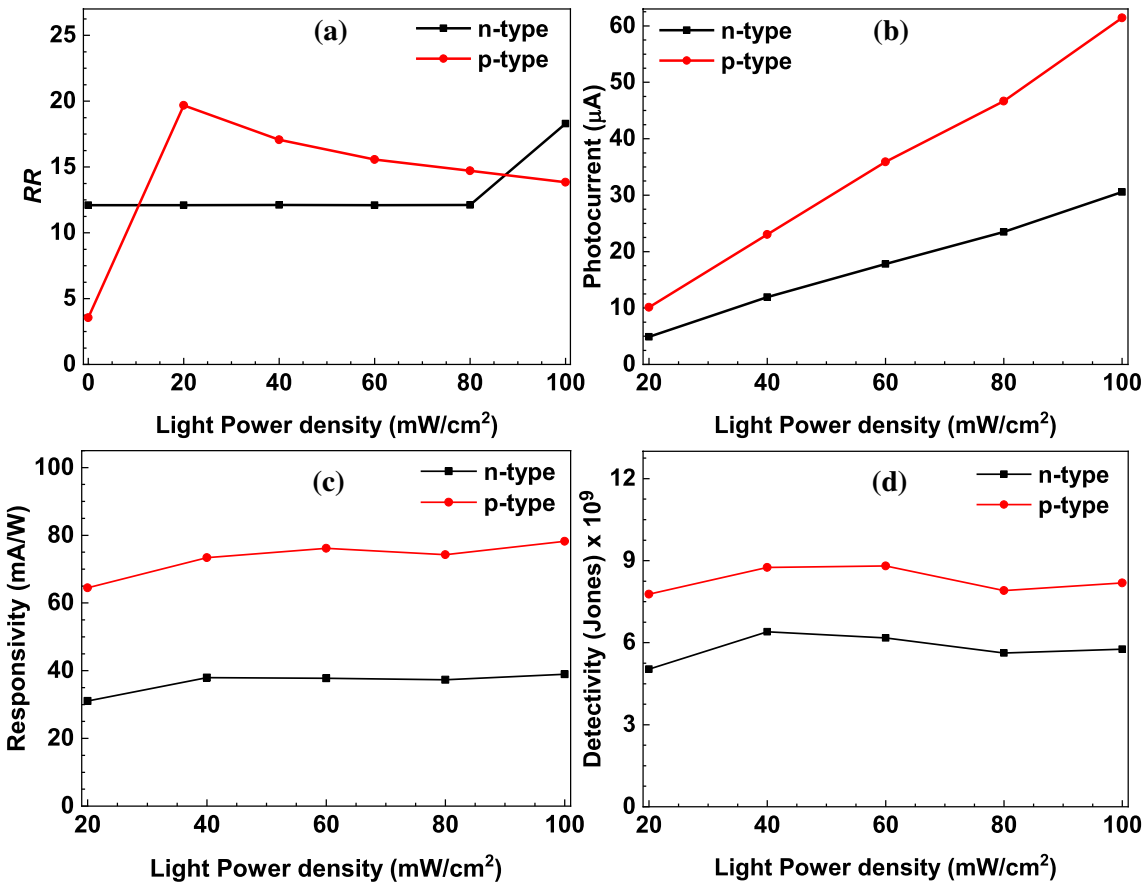

Figure 14 **a** *RR*, **b** photocurrent, **c** responsivity, and **d** detectvity profiles of the Al/PANI–silicene/*n*-Si and Al/PANI–silicene/*p*-Si photodiodes depending on the light power densities.

photodiodes align well with the existing literature on photodiodes [74–76].

Conclusion

The PANI-silicene composites were synthesized and used as interlayers of Al and both *p*-type and *n*-type silicon to manufacture Al/PANI–silicene/*p*-Si and Al/PANI–silicene/*n*-Si photodiodes. While the XRD revealed the crystalline nature of the silicene clearly, the SEM/EDS analysis confirmed the deposition of the PANI-silicene layer on Si. *I–V* and *I–t* plots of the Al/PANI–silicene/*p*-Si and Al/PANI–silicene/*n*-Si photodiodes were obtained for different light power densities from dark to 100 mW/cm^2. The diode parameters were calculated by Cheung and Norde methods, and TE theory to validate the series resistance, barrier height, and ideality factor of the photodiodes. While the ideality factor values were obtained as 5.49 and 1.48 for Al/PANI–silicene/*n*-Si and Al/PANI–silicene/*p*-Si photodiodes, the values of barrier height were obtained as 0.70 and 0.83 eV, respectively. The Al/PANI–silicene/*p*-Si photodiode exhibited photodiode characteristics at the negative voltage region and phototransistor characteristics at the positive voltage region. The basic detector properties were also calculated from *I–t* characteristics, and results were discussed in detail for PANI–silicene interfacial-based photodiodes. While the responsivity level of the Al/PANI–silicene/*n*-Si is around 10^3 mA/W, the Al/PANI–silicene/*p*-Si photodiode has a 10^2 mA/W level. The photodiodes can be a good candidate for photodetection applications.

Acknowledgements

This study was supported by the Scientific and Technological Research Council of Turkey (TUBITAK), and the authors thanked financial support for Project 122N962.

Author contributions

AK was involved in conceptualization, investigation, writing—original draft, and editing. DEY helped with writing—reviewing, and editing and also participated in supervision. NT was responsible for the investigation, writing—reviewing, and editing. MY took part in conceptualization, investigation, and writing—reviewing.

Funding

Open access funding provided by the Scientific and Technological Research Council of Türkiye (TÜBİTAK). Open access funding provided by the Scientific and Technological Research Council of Türkiye (TÜBİTAK).

Data availability

All data presented in this article will be available upon reasonable request from Dilber Esra YILDIZ as the corresponding author: desrayildiz@hitit.edu.tr.

Declarations

Conflict of interest The authors declare that they have no known conflicts of interest competing interests or personal relationships that could have appeared to influence the work reported in this paper.

References

[1] Sone J, Yamagami T, Aoki Y, Nakatsuji K, Hirayama H (2014) Epitaxial growth of silicene on ultra-thin Ag(111) films. New J Phys 16:095004. https://doi.org/10.1088/1367-2630/16/9/095004

[2] Şahin H, Cahangirov S, Topsakal M, Bekaroglu E, Akturk E, Senger RT, Ciraci S (2009) Monolayer honeycomb structures of group-IV elements and III-V binary compounds: first-principles calculations. Phys Rev B 80:155453. https://doi.org/10.1103/PhysRevB.80.155453

[3] Lew Yan Voon LC (2016) Physical properties of silicene. In: Silicence structure, properties and applications, vol 235. Springer Verlag, pp 3–33

[4] Dzade NY, Obodo KO, Adjokatse SK, Ashu AC, Amankwah E, Atiso CD, Bello AA, Igumbor E, Nzabarinda SB, Obodo JT et al (2010) Silicene and transition metal based materials: prediction of a two-dimensional piezomagnet. J Phys Condens Matter 22:375502. https://doi.org/10.1088/0953-8984/22/37/375502

[5] Gian G, Guzmán-Verri, Lew Yan Voon LC (2007) Electronic structure of silicon-based nanostructures. Phys Rev B 76:075131. https://doi.org/10.1103/PhysRevB.76.075131

[6] Yang X, Ni J (2005) Electronic properties of single-walled silicon nanotubes compared to carbon nanotubes. Phys Rev B 72:195426. https://doi.org/10.1103/PhysRevB.72.195426

[7] Huang B, Deng HX, Lee H, Yoon M, Sumpter BG, Liu F, Smith SC, Wei SH (2014) Exceptional optoelectronic properties of hydrogenated bilayer silicene. Phys Rev X 4:021029. https://doi.org/10.1103/PhysRevX.4.021029

[8] Kharadi MA, Malik GFA, Khanday FA, Shah KA, Mittal S, Kaushik BK (2020) Review—silicene: from material to device applications. ECS J Solid State Sci Technol 9:115031. https://doi.org/10.1149/2162-8777/abd09a

[9] Jaymand M (2013) Recent progress in chemical modification of polyaniline dedicated to Professor Dr Ali Akbar Entezami. Prog Polym Sci 38:1287–1306

[10] Bhadra S, Khastgir D, Singha NK, Lee JH (2009) Progress in preparation, processing and applications of polyaniline. Prog Polym Sci 34:783–810

[11] Hazar Apaydin D, Esra Yildiz D, Cirpan A, Toppare L (2013) Optimizing the organic solar cell efficiency: role of the active layer thickness. Sol Energy Mater Sol Cells 113:100–105. https://doi.org/10.1016/j.solmat.2013.02.003

[12] Yu P, Feng G, Li J, Li C, Xu Y, Xiao C, Li W (2020) A selenophene substituted double-cable conjugated polymer enables efficient single-component organic solar cells. J Mater Chem C 8:2790–2797. https://doi.org/10.1039/C9TC06667E

[13] He X, Gao B, Wang G, Wei J, Zhao C (2013) A new nanocomposite: carbon cloth based polyaniline for anelectrochemical supercapacitor. Electrochim Acta 111:210–215. https://doi.org/10.1016/j.electacta.2013.07.226

[14] Wang Q, Qin Y, Li M, Ye L, Geng Y (2020) Molecular engineering and morphology control of polythiophene:nonfullerene acceptor blends for high-performance solar cells. Adv Energy Mater 10:2002572. https://doi.org/10.1002/aenm.202002572

[15] Bejbouj H, Vignau L, Miane JL, Olinga T, Wantz G, Mouhsen A, Oualim EM, Harmouchi M (2010) Influence of the nature of polyaniline-based hole-injecting layer on polymer light emitting diode performances. Mater Sci Eng B Solid-State Mater Adv Technol 166:185–189. https://doi.org/10.1016/j.mseb.2009.09.032

[16] Song E, Choi JW (2014) Self-calibration of a polyaniline nanowire-based chemiresistive ph sensor. Microelectron Eng 116:26–32. https://doi.org/10.1016/j.mee.2013.10.014

[17] Alonso JL, Ferrer JC, Cotarelo MA, Montilla F, de Ávila SF (2009) Influence of the thickness of electrochemically deposited polyaniline used as hole transporting layer on the behaviour of polymer light-emitting diodes. Thin Solid Film 517:2729–2735. https://doi.org/10.1016/j.tsf.2008.10.145

[18] Talwar V, Singh O, Singh RC (2014) ZnO Assisted polyaniline nanofibers and its application as ammonia gas sensor. Sens Actuators B Chem 191:276–282. https://doi.org/10.1016/j.snb.2013.09.106

[19] Yıldız DE, Cevher D, Yasa M, Cirpan A, Toppare L (2022) Selenophene-containing conjugated polymers for supercapacitor electrodes. J Polym Sci 60:109–121. https://doi.org/10.1002/pol.20210746

[20] Ezzati N, Asadi E, Abdouss M, Ezzati MH (2017) Polyaniline nano-/micromaterials–based blends and composites. In: Visakh, PM (eds), Polyaniline blends, composites, and nanocomposites. Elsevier, pp 95–115

[21] Babel V, Hiran BL (2021) A review on polyaniline composites: synthesis, characterization, and applications. Polym Compos 42:3142–3157

[22] Beygisangchin M, Rashid SA, Shafie S, Sadrolhosseini AR, Lim HN (2021) Preparations, properties, and applications of polyaniline and polyaniline thin films—a review. Polymers (Basel) 13:2003. https://doi.org/10.3390/polym13122003

[23] Mozafari M, Chauhan NPS (2019) Fundamentals and emerging applications of polyaniline. Elsevier, p 308

[24] Gupta SC, Preier H (1984) Schottky barrier photodiodes. In: Metal-semiconductor schottky barrier junctions and their applications. Springer, Boston, MA, pp 191–218

[25] Diels W, Steyaert M, Tavernier F (2020) 1310/1550 Nm Optical receivers with Schottky photodiode in bulk CMOS. IEEE J Solid-State Circuits 55:1776–1784. https://doi.org/10.1109/JSSC.2020.2991517

[26] Ji X, Yin X, Yuan Y, Yan S, Li X, Ding Z, Zhou X, Zhang J, Xin Q, Song A (2023) Amorphous Ga_2O_3 Schottky photodiodes with high-responsivity and photo-to-dark current ratio. J Alloys Compd 933:167735. https://doi.org/10.1016/j.jallcom.2022.167735

[27] Yakimov EB, Polyakov AY, Shchemerov IV, Smirnov NB, Vasilev AA, Kochkova AI, Vergeles PS, Yakimov EE, Chernykh AV, Xian M et al (2021) On the nature of photosensitivity gain in Ga_2O_3 Schottky diode detectors: effects of hole trapping by deep acceptors. J Alloys Compd 879:160394. https://doi.org/10.1016/j.jallcom.2021.160394

[28] Karadeniz S, Barış B, Karadeniz H, Yıldırım M (2022) The production of organic photodetectors and determination of electrical properties for optical sensor applications. Gazi Univ J Sci Part A Eng Innov 9:267–275. https://doi.org/10.54287/gujsa.1141142

[29] Kocyigit A, Yıldız DE, Hussaini AA, Kose DA, Yıldırım M (2023) Cu and Mn centered nicotinamide/nicotinic acid complexes for interlayer of Schottky photodiode. Curr Appl Phys 45:53–63. https://doi.org/10.1016/j.cap.2022.11.001

[30] Kaya A, Marıl E, Altındal Ş, Uslu İ (2016) The comparative electrical characteristics of Au/n-Si (MS) diodes with and without a 2% graphene cobalt-doped Ca3Co4Ga0.001Ox interfacial layer at room temperature. Microelectron Eng 149:166–171. https://doi.org/10.1016/J.MEE.2015.10.012`

[31] Yıldırım F, Orhan Z (2023) Aydoğan UV-visible photovoltaic detector based on biomaterial-inorganic semiconductor in the propolis/n-Si heterojunction configuration. Mater Res Bull 159:112113. https://doi.org/10.1016/j.materresbull.2022.112113

[32] Havigh RS, Chenari HM, Yıldırım F, Orhan Z (2023) Aydoğan improving the performance of the self-powered polymer-based UV/Vis photodetectors via carbon fibers. Phys Scr 98:015831. https://doi.org/10.1088/1402-4896/acab9e

[33] Gencer Imer A, Dere A, Kaya E, Al-Sehemi AG, Dayan O, Al-Ghamdi AA, Yakuphanoglu F (2023) The photodetection properties of a ruthenium electro-optic device for organic material-based device industry. Opt Mater (Amst) 142:114085. https://doi.org/10.1016/j.optmat.2023.114085

[34] Baytemir G, Taşaltın N, Karaca B, Karakuş S, Gürsu G, Barış B, Yıldız DE (2023) PANI: silicene nanocomposites based non-enzymatic electrochemical voltammetric sensor for dopamine detection. J Mater Sci Mater Electron 34:1–10. https://doi.org/10.1007/s10854-023-10809-9

[35] Zeynali S, Taghizadeh MT (2019) Highly efficient TiO2/AgBr/PANI heterojunction with enhanced visible light photocatalytic activity towards degradation of organic dyes. J Mater Sci Mater Electron 30:17020–17031. https://doi.org/10.1007/s10854-019-02036-y

[36] Liu H, Gao J, Zhao J (2013) Silicene on substrates: a way to preserve or tune its electronic properties. J Phys Chem C 117:10353–10359. https://doi.org/10.1021/jp311836m

[37] Liu H, Gao J, Zhao J (2014) Silicene on substrates: interaction mechanism and growth behavior. J Phys Conf Ser 491:012007. https://doi.org/10.1088/1742-6596/491/1/012007

[38] Huang WQ, Liu SR, Peng HY, Li X, Huang ZM (2020) Synthesis of new silicene structure and its energy band properties*. Chinese Phys B 29:084202. https://doi.org/10.1088/1674-1056/ab942c

[39] Borlido P, Rödl C, Marques MAL, Botti S (2018) The ground state of two-dimensional silicon. 2D Mater 5:035010. https://doi.org/10.1088/2053-1583/aab9ea

[40] Yıldız DE, Baytemir G, Taşaltın N, Karakuş S, Gürsu G, Köse DA (2023) PANI: Ni(Leu)2 based non-enzymatic electrochemical dopamine sensor. Phys Scr 98:125906. https://doi.org/10.1088/1402-4896/ad05ef

[41] Sharma S, Singh S, Khare N (2016) Enhanced photosensitization of zinc oxide nanorods using polyaniline for efficient photocatalytic and photoelectrochemical water splitting. Int J Hydrog Energy 41:21088–21098. https://doi.org/10.1016/j.ijhydene.2016.08.131

[42] Tchalala MR, Ali MA, Enriquez H, Kara A, Lachgar A, Yagoubi S, Foy E, Vega E, Bendounan A, Silly MG et al (2013) Silicon sheets by redox assisted chemical exfoliation. J Phys Condens Matter 25:442001. https://doi.org/10.1088/0953-8984/25/44/442001

[43] Li S, Wu Q, Ding H, Wu S, Cai X, Wang R, Xiong J, Lin G, Huang W, Chen S et al (2023) High gain, broadband p-WSe2/n-Ge van der waals heterojunction phototransistor with a Schottky barrier collector. Nano Res 16:5796–5802. https://doi.org/10.1007/s12274-022-5081-0

[44] Lee SK, Zetterling CM, Östling M (2001) Schottky barrier height dependence on the metal work function for P-Type 4H-silicon carbide. J Electron Mater 30:242–246. https://doi.org/10.1007/s11664-001-0023-1

[45] Çankaya G, Uçar N (2004) Schottky barrier height dependence on the metal work function for P-Type Si Schottky diodes. Zeitschrift fur Naturforsch-Sect A J Phys Sci 59:795–798. https://doi.org/10.1515/zna-2004-1112

[46] Siad M, Keffous A, Mamma S, Belkacem Y, Menari H (2004) Correlation between series resistance and parameters of Al/n-Si and Al/p-Si Schottky barrier diodes. Appl

Surf Sci 236:366–376. https://doi.org/10.1016/j.apsusc.2004.05.009

[47] Cifci OS, Kocyigit A, Sun P (2018) Perovskite/p-Si photodiode with ultra-thin metal cathode. Superlattices Microstruct 120:492–500. https://doi.org/10.1016/J.SPMI.2018.06.009

[48] Kocyigit A, Yılmaz M, Aydoğan Ş, İncekara Ü (2019) The effect of measurements and layer coating homogeneity of AB on the Al/AB/p-Si devices. J Alloys Compd 790:388–396. https://doi.org/10.1016/j.jallcom.2019.03.179

[49] Turut A, Efeoğlu H (2021) Thermal sensitivity from current-voltage-measurement temperature characteristics in Au/n-GaAs Schottky contacts. Turkish J Phys 45:268–280. https://doi.org/10.3906/fiz-2108-15

[50] Karabulut A, Orak İ, Canlı S, Yıldırım N, Türüt A (2018) Temperature-dependent electrical characteristics of Alq3/p-Si heterojunction. Phys B Condens Matter 550:68–74. https://doi.org/10.1016/j.physb.2018.08.029

[51] Gumus I, Aydogan S (2021) Thermal sensing capability of metal/composite-semiconductor framework device with the low barrier double Gaussian over wide temperature range. Sens Actuators A Phys 332:113117. https://doi.org/10.1016/j.sna.2021.113117

[52] Çaldıran Z (2021) Modification of Schottky barrier height using an inorganic compound interface layer for various contact metals in the metal/p-Si device structure. J Alloys Compd 865:158856. https://doi.org/10.1016/j.jallcom.2021.158856

[53] Doğan H (2022) Parameter estimation of AI/p-Si Schottky barrier diode using different meta-heuristic optimization techniques. Symmetry (Basel) 14:2389. https://doi.org/10.3390/sym14112389

[54] Mayimele MA, Van Rensburg JPJ, Auret FD, Diale M (2016) Analysis of temperature-dependant current-voltage characteristics and extraction of series resistance in Pd/ZnO Schottky barrier diodes. Phys B Condens Matter 480:58–62. https://doi.org/10.1016/j.physb.2015.07.034

[55] Orak İ, Kocyiğit A, Karataş Ş (2018) The analysis of the electrical and photovoltaic properties of Cr/p-Si structures using current-voltage measurements. SILICON 10:2109–2116. https://doi.org/10.1007/s12633-017-9731-x

[56] Kocyigit A, Yilmaz M, İncekara Ü, Aydogan S, Kacus H (2021) Molecular engineering for donor electron to enhance photodiode properties of Co/n-Si and Co/p-Si structures: the effect of hematoxylin interface. Optik (Stuttg) 242:167314. https://doi.org/10.1016/J.IJLEO.2021.167314

[57] Cuneyt Haciismailoglu M, Ahmetoglu M, Haciismailoglu M, Alper M, Batmaz T (2022) Electrical and optical properties of Schottky diodes fabricated by electrodeposition of Ni Films on N-GaAs. Sens Actuators A Phys 347:113931. https://doi.org/10.1016/j.sna.2022.113931

[58] Barkhordari A, Mashayekhi HR, Amiri P, Altındal Ş, Azizian-Kalandaragh Y (2024) Optoelectric response of schottky photodiode with a pvp: zntio3 nanocomposite as an interfacial layer. Opt Mater (Amst) 148:114787. https://doi.org/10.1016/j.optmat.2023.114787

[59] Wang Y, Yang S, Lambada DR, Shafique S (2020) A graphene-silicon Schottky photodetector with graphene oxide interlayer. Sens Actuators, A Phys 314:112232. https://doi.org/10.1016/j.sna.2020.112232

[60] Dhibar S, Roy A, Sarkar T, Das P, Karmakar K, Bhattacharjee S, Mondal B, Chatterjee P, Sarkar K, Ray SJ et al (2024) Rapid semiconducting supramolecular Mg(II)-metallohydrogel: exploring its potential in nonvolatile resistive switching applications and antiseptic wound healing properties. Langmuir 40:179–192. https://doi.org/10.1021/acs.langmuir.3c02298

[61] Karmakar K, Roy A, Dhibar S, Majumder S, Bhattacharjee S, Rahaman SKM, Saha R, Chatterjee P, Ray SJ, Saha B (2023) Exploration of a wide bandgap semiconducting supramolecular Mg(II)-metallohydrogel derived from an aliphatic amine: a robust resistive switching framework for brain-inspired computing. Sci Rep 13:22318. https://doi.org/10.1038/s41598-023-48936-2

[62] Karmakar K, Roy A, Dhibar S, Majumder S, Bhattacharjee S, Mondal B, Rahaman SKM, Saha R, Ray SJ, Saha B (2023) Instantaneous gelation of a self-healable wide-bandgap semiconducting supramolecular Mg(II)-metallohydrogel: an efficient nonvolatile memory design with supreme endurance. ACS Appl Electron Mater 5:3340–3349. https://doi.org/10.1021/acsaelm.3c00376

[63] Bertoldo LHT, Nogueira GL, Vieira DH, Klem MS, Ozório MS, Alves N (2022) Analytical study of a solution-processed diode based on ZnO nanoparticles using multi-walled carbon nanotubes as Schottky contact. J Mater Sci Mater Electron 33:14508–14518. https://doi.org/10.1007/s10854-022-08371-x

[64] Cheung SK, Cheung NW (1986) Extraction of Schottky diode parameters from forward current-voltage characteristics. Appl Phys Lett 49:85. https://doi.org/10.1063/1.97359

[65] Orhan Z, Yilmaz M, Aydogan S, Taskin M, Incekara U (2021) Improving light-sensing behavior of Cu/n-Si photodiode with human serum albumin: microelectronic and dielectric characterization. Optik (Stuttg) 241:167069. https://doi.org/10.1016/j.ijleo.2021.167069

[66] Aldemir DA (2020) Analysis of current-voltage and capacitance-voltage characteristics of Zr/p-Si Schottky diode with high series resistance. Mod Phys Lett B 34:2050095. https://doi.org/10.1142/S0217984920500955

[67] Rao LD, Reddy VR (2016) Electrical parameters and series resistance analysis of Au/Y/p-InP/Pt schottky barrier diode at room temperature. In: Proceedings of the AIP Conference Proceedings, vol 1731. AIP Publishing LLC, p 120020

[68] Gullu HH, Yıldız DE, Kose DA, Yıldırım M (2022) Si-based photosensitive diode with novel Zn-doped nicotinate/nicotinamide mixed complex interlayer. Mater Sci Semicond Process 147:106750. https://doi.org/10.1016/j.mssp.2022.106750

[69] Wang Y, Zou X, Zhu J, Zhang C, Cheng J, Wang J, Wang X, Li X, Song K, Ren B et al (2022) Investigation of the photoresponse and time-response characteristics of HDA-BiI5-based photodetectors. Materials (Basel) 15:321. https://doi.org/10.3390/ma15010321

[70] Yükseltürk E, Surucu O, Terlemezoglu M, Parlak M, Altındal Ş (2021) Illumination and voltage effects on the forward and reverse bias current-voltage (I-V) characteristics in In/In2S3/p-Si photodiodes. J Mater Sci Mater Electron 32:21825–21836. https://doi.org/10.1007/s10854-021-06378-4

[71] Ocaya RO, Dere A, Al-Sehemi AG, Al-Ghamdi AA, Soylu M, Yakuphanoglu F (2017) Analysis of photoconductive mechanisms of organic-on-inorganic photodiodes. Phys E Low-Dimens Syst Nanostruct 93:284–290. https://doi.org/10.1016/j.physe.2017.06.024

[72] Xu J, Liu T, Hu H, Zhai Y, Chen K, Chen N, Li C, Zhang X (2020) Design and optimization of tunneling photodetectors based on graphene/Al2O3/silicon heterostructures. Nanophotonics 9:3841–3848. https://doi.org/10.1515/nanoph-2019-0499

[73] Crisci T, Moretti L, Gioffrè M, Iodice M, Coppola G, Casalino M (2020) Integrated Er/Si Schottky photodetectors on the end facet of optical waveguides. J Eur Opt Soc 16:1–8. https://doi.org/10.1186/s41476-020-00127-6

[74] Shafique S, Yang S, Wang Y, Woldu YT, Cheng B, Ji P (2019) High-performance photodetector using urchin-like hollow spheres of vanadium pentoxide network device. Sens Actuators A Phys 296:38–44. https://doi.org/10.1016/j.sna.2019.07.003

[75] Ren B, Liao M, Sumiya M, Huang J, Wang L, Koide Y, Sang L (2019) Vertical-Type Ni/GaN UV photodetectors fabricated on free-standing GaN substrates. Appl Sci 9:2895. https://doi.org/10.3390/app9142895

[76] Gao XD, Fei GT, Xu SH, Zhong BN, Ouyang HM, Li XH, De ZL (2019) Porous Ag/TiO2-Schottky-diode based plasmonic hot-electron photodetector with high detectivity and fast response. Nanophotonics 8:1247–1254. https://doi.org/10.1515/nanoph-2019-0094